Localized aerosol-assisted CVD of nanomaterials for the fabrication of monolithic gas sensor microarrays

F. E. Annanouch [a], I. Gràcia [b], E. Figueras [b], E. Llobet [a], C. Cané [b], S. Vallejos [b, c, *]

[a]MINOS-EMaS, Department d'Enginyeria Electrónica, Universitat Rovira i Virigili, Tarragona, Spain
[b]Instituto de Microelectrónica de Barcelona (IMB-CNM), CSIC, Barcelona, Spain
[c]SIX Research Center, Faculty of Electrical Engineering and Communication, Brno University of Technology, Brno, Czech Republic

Abstract.

The self-heating capability of MEMS-based devices is used to grow locally into the sensing active area of monolithic gas sensor microarrays differently functionalized materials via aerosol-assisted CVD. Results derived from SEM, TEM, XRD and Raman demonstrate the integration of non-functionalized (WO_{3-x}) and functionalized nanostructures with gold or platinum NPs (WO_{3-x}/Au and WO_{3-x}/Pt) into the array. Tests of these microarrays towards various concentrations of reducing gases show stable and reproducible responses, with the highest responses (R) for WO_{3-x} to carbon monoxide (e.g. R=4.3 to 80 ppm), for WO_{3-x}/Au to ethanol (e.g. R=7 to 80 ppm) and for WO_{3-x}/Pt to hydrogen (e.g. R=3.6 to 80 ppm). Principal component analysis of the sensor response replicates to each gas and concentration suggest that the differences in the sensing properties of each element of the array provide the complementary information to discriminate H_2 and EtOH from CO.

Keywords: Nanostructures, localized synthesis, gas sensor arrays, AACVD, tungsten oxide, functionalization

*Corresponding author
SIX Research Center, Faculty of Electrical Engineering and Communication, Brno University of Technology, Technicka 12, CZ-61600 Brno, Czech Republic.
Tel: +420 541 146 153, fax: +420 541 146 298
E-mail addresses: vargas@feec.vutbr.cz (S. Vallejos)

1. Introduction

In the last decade, MEMS-based gas microsensors have provided miniaturization making possible the inclusion of on-chip circuitry and the replica of these devices to build microsensor arrays within a single chip. Moreover, arrays consisting of different partially selective sensors have demonstrated to improve identification and quantification of gaseous analytes [1]. Against a host of competing enabling technologies for gas sensing, chemoresistive sensors are considered as good candidates to form sensor arrays, owing to their simple architecture with electrical properties and readout interface circuits less complex compared to other sensors (e.g. optical, mass-sensitive) [1b]. Chemoresistive gas microsensors based on MEMS technology are generally comprised of a thin suspended membrane, which contains the sensing material on the top (usually a metal oxide (MOX) or conductive- polymer), microelectrodes (to measure the electrical resistance changes of the sensing material) and microheating elements (only in MOX-based sensors to offer the MOX the appropriate thermal environment for the gas-solid interactions) [1b; 1d]. The suspended membrane provide good thermal isolation between the active sensing area and the complementary electronics, which results in their characteristic low power consumption and allows for their use in temperature-pulsed operating mode improving selectivity and response time [2].

High functional nanostructured materials (e.g. nanowires, nanotubes and nanorods) have demonstrated significantly different optical, electrical and magnetic properties compared to their bulk counterparts [3]. Nowadays, the integration of these structures with micro/nano devices represents a technological challenge, particularly due to the stringent thermal environments required to produce these materials, which lead to incompatibilities with the complementary electronics of the device. Earlier, we have addressed the issues associated with the integration of nanostructures (NSs) in individual MEMS-based

microsensors by achieving NSs (either MOX-NSs or metal nanoparticles (NPs) functionalized MOX-NSs) via conventional aerosol-assisted chemical vapor deposition (AACVD) in a 'hot-wall' reactor. These microsensors showed high sensitivities to hydrogen (H_2), ethanol (EtOH) and carbon monoxide (CO) and enhanced selectivity when correlating their responses using principal component analysis [4]. Although, the selective integration of these structures in microsensor arrays within a single-chip was not achieved by this method, because of the integration of different structures into arrays requires various thermal cycles (one per each integrated material), which inevitably causes the introduction of contaminants and/or the structural transformation of the preceding NSs. The fabrication of microsensor arrays with different sensing elements is of particular importance as single sensors based on MOX commonly lack of selectivity, which is the major reason these sensors do not reach certain markets [1b; 1d; 5]. Technological improvements in the fabrication of microsensor arrays will enable more progress in the development of new generation of key miniaturized/integrated devices, such as electronic noses, for their application in distinct areas, which may include indoor air-quality monitoring, environmental- quality monitoring, medical care, and food quality control, among others [1b; 6].

Recently, localized heating for CVD synthesis has emerged as a viable technique to confine the required thermal environment for both the decomposition of the vapor-phase reactants and the growth kinetics of NSs to a microscale area [7], with the promise to reduce significantly the power consumption of high temperature 'hot-wall' reactors (as microheaters offer faster temperature response with low power consumption) and the processing time (as the integration of nanostructures via localized heating avoid the use of masks or other intermediate thermal process steps for their integration), which may reduce the costs of the process. The use of localized heating for CVD is expected to

increase deposition efficiency and reduce contamination avoiding deposition of precursors on the reaction chamber walls. CVD via localized heating has been mainly used for CNT synthesis [7], and although some attempts have also been reported for the synthesis of other materials, e.g. MOX-NSs [8], the impact of a non-isothermal environment in the properties of materials remains largely unexplored, and some drawbacks of traditional CVD, such as the high onset temperatures (up to 1000 ºC or more) for formation of nanostructures, the need of volatile precursors and the requirement of vacuum environment, are still present [9]. AACVD, as an evolution of conventional CVD, has the peculiarity of forming functional NSs at relatively low temperatures (400 ºC), at atmospheric pressure, high deposition rates and without requiring the use of volatile precursors [4b; 10], which highlights the advantages of this method for the vapor-phase synthesis of MOX-NSs via localized heating [11].

Here, localized AACVD is developed using the self-heating capability of MEMS-based microsensors to fabricate an array of different sensing elements (non-functionalized and functionalized tungsten oxide with gold and platinum NPs) in a single-chip, and produce microsystems with potential enhanced selectivity. Tungsten oxide is used due to its promising properties for gas-sensing applications. Currently, this material is widely applied for the detection of nitrous oxides, finding use in many commercial products usually in the form of thick film [12]. In addition, the literature show that this material, both in its intrinsic form and when functionalized with metal NPs (e.g. Au, Pt, Pd, Ag), present high potential for detecting other gaseous species such as O_3 [13], H_2 [14], H_2S [15], SO_2 [15b], and EtOH [14b; 16].

2. Experimental

MEMS-based microsensor platforms (Figure 1) consisted of a suspended membrane (1×1 mm) of Si_3N_4 (300 nm thick), containing a $POCl_3$-doped polysilicon meander

shaped resistive heater (covering an area of 400×400 μm, 0.47 μm thick, 16 Ω/sq, and TCR: 6.79×10^{-4}/ºC) and platinum electrodes (covering an area of 400×400 μm, 0.2 μm thick, electrode gap: 50 μm, and aspect ratio of ~13), isolated by an interlevel silicon oxide layer (800 nm thick), were produced at wafer-level employing various microfabrication steps, including implantation, photolithography, metallization, lift-off and rear side etching of the substrate to define the membranes. Each chip comprised an array of four microsensors bounded and mounted on a standard TO-8 package [17].

Electrothermal simulations of the microsensor were carried out using the Joule Heating and Thermal Expansion model of COMSOL Multiphysics 4.0a (Figure 2). These simulations were performed adjusting the material properties to those obtained from the device fabrication tests, including the Thermal Coefficient of Resistance (TCR) for the polysilicon microheaters, that was obtained via measures of the electrical resistance of the heaters (630 Ω at RT and 750 Ω at 300 °C) using a multimeter (Keithley 2400) and a temperature controlled furnace.

Tungsten oxide NSs were synthesized on the packaged-microsensors via localized AACVD of tungsten hexacarbonyl (20 mg, $W(CO)_6$, Sigma-Aldrich, ≥97%) dissolved in methanol (5 ml, Sigma-Aldrich, ≥99.6%). Similarly, tungsten oxide NSs functionalized with gold and platinum NPs were co-deposited via localized AACVD of tungsten hexacarbonyl (20 mg, $W(CO)_6$, Sigma–Aldrich, ≥97%) with either tetrachloroauric acid trihydrate (1 mg, $HAuCl_4•3H_2O$, Sigma–Aldrich, 99.9%) or hexachloroplatinic acid hydrate (1 mg, $H_2PtCl_6•xH_2O$, Sigma–Aldrich, 99.9%) dissolved in methanol (5 ml, Sigma-Aldrich, ≥99.6%). In this work, the evaporation and reaction of the aerosol droplets was promoted by using the self-heating capability of the MEMS-based microsensor platforms and maintaining the reaction chamber at room temperature, unlike our previous reports in which a ‘hot wall’ reactor was used [4b]. Thus, the packaged

microsensors (Figure 1c) were placed in a reactor made of a non-conductive material, provided with electrical contacts for biasing the microheaters, and the aerosol droplets were carried to the heated surface by a controlled nitrogen flow (200 sccm). After material deposition, localized annealing of the films was carried out at 580 ºC for 2 h with a constant flow of synthetic air (50 sccm, Praxair, 99.99%). The temperature of the microsensor, both for deposition and annealing of the NSs, was adjusted by applying a constant voltage to the microheater integrated in the microsensor. AACVD was carried out using various temperatures, between 300 ºC and 580 ºC, in order to study the temperature dependency of the film morphology.

The morphology and the elemental composition of the films were examined using Scanning Electron Microscopy and Energy Dispersive X-ray Spectroscopy (SEM and EDX — Carl Zeiss, Auriga Series), respectively. The NSs were also characterized using Transmission Electron Microscopy (TEM — Jeol 1011, 100 kV). TEM samples were prepared by sonication of the membrane in methanol, after having removed it mechanically from the device. The film structure was examined using X-Ray Diffraction (XRD — Bruker, AXS D8- Advance, Cu Kα radiation operated at 40 kV and 40 mA) and the chemical structure using RAMAN (Renishaw in Via, laser of 514 nm, ion argon — Novatech, 25 mW).

Gas sensing tests were carried out towards various analytes by monitoring the electrical resistance changes of the films, at sensor operating temperatures between 160 and 390 ºC (in intervals of ~60 °C), using a multimeter (Data Acquisition/Switch Unit — Agilent 34970A) configured with 20-channels relay multiplexer. The sensors were exposed to each analyte for 10 minutes in a continuous flow (200 sccm) test chamber (280 cm^3) with synthetic air as carrier gas (Praxair, 99.99%) [4b]. Subsequently, the chamber was purged with synthetic air until the initial baseline resistance was recovered. Before each test to

each analyte and operating temperature, the sensors were stabilized 30 minutes in the carrier gas. The sensor response (R) was defined as R=Ra/Rg, where Ra represents the sensor resistance in synthetic air at stationary state and Rg is the sensor resistance after 10 minutes of gas exposure. The response time was defined as the time required for the sensor to reach 90% of the sensor response, and the recovery time as the time required to reach 10% of the initial baseline resistance after the analyte was purged. Calibrated cylinders of hydrogen (H_2, Carburos Metálicos, 1000 ppm), carbon monoxide (CO, Carburos Metálicos, 1000 ppm) and ethanol (EtOH, Carburos Metálicos, 100 ppm) were mixed with pure synthetic air (Praxair, 99.99%) in order to obtain the desired concentration (20, 80, 200 and 500 ppm for H_2; 40, 80, 200 and 500 ppm for CO; and 20, 40, 60, 80 ppm for EtOH). These concentrations were chosen in agreement to our previous studies on the use of tungsten oxide nanostructures grown via 'hot-wall' reactor in order to have a reference for the validation of these sensors, fabricated via localized AACVD. The gas testing results shown in section 3 were recorded using the same array of non-functionalized and functionalized sensors with gold and platinum NPs for each testing condition (i.e. analyte, concentration, and temperature). The whole testing period spanned for this array was two months during which the array was alternatively tested to the analytes at different concentrations and operating temperatures. Each measurement was replicated five times and during this test period, the array of sensors accumulated a total of 250 h of operation.

Humidity tests towards CO were carried out using a gas mixing system (Environics, Series 4000), which controls the relative humidity (RH) and mix automatically the analyte (i.e. CO) diluted in synthetic air with humidity. The total flows and exposition times remained the same than those used for gas testing in synthetic air.

3. Results and Discussion

3.1.Thermal and electrical characteristics of the microheaters

To evaluate the temperature distribution at the microsensor, electro-thermal simulations were performed biasing the heater at various voltages. Overall, results obtained from the simulations using different voltages showed a symmetric temperature profile along the membrane and a uniform thermal distribution at the sensing-active area of the microsensor, which is attributed to the double loop design of the microheater (Figure 2). Prior to AACVD and annealing of the sensing films (i.e. non-functionalized and either Au- or Pt- functionalized tungsten oxide NSs), the membranes were subjected to an aging process at 580 °C using the self-heating capability of the microheaters in order to thermodynamically relax and stabilize the multiple layers comprising the membrane. During this process, the electrical resistance of the microheaters experienced a drift up to 12%, respect to the initial electrical resistance, reaching stabilization after 45 min. Subsequent intermittent tests of the microheater during AACVD, annealing process, and gas testing showed no drift of the microheaters' electrical resistance.

3.2.Localized AACVD of the sensing films

Localized AACVD of $W(CO)_6$ and $W(CO)_6$ with either $HAuCl_4 \cdot 3H_2O$ or $H_2PtCl_6 \cdot xH_2O$ at various temperatures (between 300 ºC and 580 ºC) resulted in the formation of adherent uniform films confined on the membrane. These films were characterized by a dark color as-deposited, becoming white after localized annealing at 580 °C, which suggest a diminution of carbon residues from decomposition of the solvent used to form aerosol [18]. EDX analysis of the sensing-active area of the microsensors after AACVD indicated O/W ratios of 2.3 for as-deposited films and 2.7 for annealed films. Despite relative low sensitivity of this technique for oxygen determinations, annealed films gave consistently higher O/W ratios than the corresponding as-deposited films.

Overall, low magnification SEM imaging of the films (non-functionalized and

functionalized), for each deposition temperature studied, indicated the material grows over the membrane forming rings with different degrees of agglomeration (Figure 3a). Thus four regions are clearly distinguished, showing consistency with the temperature rings observed in the simulations (Figure 2b). At higher magnification, these regions showed particle-like morphologies, for films grown at temperatures below 540 ºC (i.e. the effective temperature in the sensing-active area of the microsensors), with a concentration of smaller particles along the sensing-active area, as opposed to the outer regions. In contrast, the films (non-functionalized and functionalized) grown at 580 ºC showed a mixture of non-aligned uniformly distributed hollow-nanotube (NTs) and nanoneedle (NNs) structures (Figure 3b, 3c) along the sensing-active area, with a modification of these structures on the subsequent temperature rings until they result in round-shaped particle films on the outermost ring. These morphological transformations result from the temperature gradients at the membrane, and are similar to those observed when growing tungsten oxide via AACVD in a 'hot wall' reactor [10a], although, it was noticed that the onset temperatures for the formation of nanostructured films are apparently higher compared to those determined before for AACVD in a 'hot-wall' reactor (e.g. 350 ºC for $W(CO)_6$ dissolved in methanol) [18-19]. The different onset temperatures for the formation of NSs using AACVD via localized heating or 'hot-wall' reactors may be related to a change in the relation between the heated volume and the residence time of the droplets within this volume, with the volume heated locally, becoming several times smaller compared to that of the 'hot-wall' reactor.

SEM imaging of the films grown at 580 °C and annealed locally at the same temperature (i.e. 580 °C) showed unchanged morphologies in both non-functionalized and functionalized films. Monitoring of the electrical resistance of the films during annealing showed an increase of resistance, which reached a stationary stage after 120 min. The

increase of the film resistance during annealing suggests a reduction of the concentration of oxygen vacancies in the structure [20]. This is in line with the higher O/W ratios determined by EDX in annealed films. TEM analysis (Figure 4) of the films removed from the membrane by sonication displayed structures with different diameters, between 20 to 350 nm, which is in agreement with the mixture of the structures (NTs and NNs) observed by SEM. The aspect ratios, estimated from the SEM and TEM images of this samples, are between 10 and 175 due to the mixture of NTs and NNs. The presence of relatively thick structures, including those coming from the membrane and the NTs, obstructed the visualization of the NPs distribution and the observation of the metal NPs incorporated in the structure. Overall, the particles, observed in the thinner structures, displayed approximately spherical morphologies, with sizes between 5–20 nm, 5–12 nm for the structures functionalized with Au and Pt, respectively, which is consistent with similar functionalized structures grown in a 'hot-wall' reactor [4b]. According to the thermal decomposition profiles of the metal precursors ($HAuCl_4$ [21] and H_2PtCl_6 [22]) used for the functionalization of tungsten oxide, metallic gold and platinum should be obtained at the temperature required for the formation of tungsten oxide NSs via localized heating.

Several depositions (15 for each material, i.e. non-functionalized and functionalized) were run at 580 °C, with good reproducibility of the morphology observed in the sensing-active area of the sensor. Consequently, these sensors (i.e. with nanostructures deposited at 580 °C) were used for the gas sensing characterization.

3.3.Sensing film structure

XRD analysis of the membranes, with the non-functionalized and functionalized tungsten oxide NSs grown onto them, are shown in Figure 5a. As the main diffractions in these patterns are close to those reported for monoclinic (ICCD card no. 72-0677) and

orthorhombic (ICCD card no. 71-0131) tungsten oxide, a clear discrimination between these phases is not straightforward from these results. However, based on previous XRD studies, in which similar tungsten oxide structures grown in 'hot-wall' reactor AACVD showed regularly monoclinic phases at similar deposition temperatures [4; 10; 18-19], it is likely the tungsten oxide structures grown via localized AACVD show the presence of a monoclinic-phase with two different stoichiometry: WO_3 (P21/n space group, a= 7.306 Å, b=7.540 Å, c=7.692 Å, and β=90.88º; ICCD card no. 72-0677) and WO_2 (P21/n space group, a= 5.575 Å, b=4.899 Å, c=5.561 Å, and β=118.86º; ICCD card no. 32-1393). The platinum and boron nitride (BN) diffraction peaks observed in the patterns come from the electrodes and the membrane, respectively. Gold diffraction peaks were not observed in the films functionalized with gold likely due to the low gold loadings incorporated. As standard XRD gives information about structural properties averaged over relatively large areas (~3 mm in x direction) [23], the XRD patterns in Figure 4a show not only the diffractions of the sensing-active area (400 µm × 400 µm) of the microsensor (Figure 1b), but also those from the material deposited in the outer rings of this area, where the morphological features of the film are degraded, hence, the presence of diffraction patterns with different stoichiometry. In this context, Raman analysis (Figure 5b) was used to determine the properties of the materials grown on the sensing-active area of the sensors. These results indicated well-defined Raman bands at 270, 326, 715 and 803 cm^{-1}. These bands fall close to the wavenumbers of the four strongest modes of monoclinic tungsten oxide [24]. The bands at 270 and 326 cm^{-1} are assigned to bending modes of the bridging oxygen, whereas the bands at 715 and 803 cm^{-1} are assigned to the stretching modes. The weak bands at around 439 cm^{-1} and the lattice modes below 200 cm^{-1} are typical bands of the crystalline tungsten oxide. These results demonstrate that the films grown onto the sensing-active area are characterized by a monoclinic-phase WO_3 and

without structural transformations due to the incorporation of gold and platinum NPs. Interestingly, Raman analysis in different points of the sensing-active area showed consistently higher intensity peaks for the functionalized film (~10 %) compared to non-functionalized films, which could indicate that the incorporation of metal NPs induces defects and oxygen vacancies in the tungsten oxide structure.

3.4.Electrical properties

The work functions of gold (4.5 – 4.8 eV) [25], platinum (5.2 – 5.4 eV) [25], and tungsten oxide (4.3 – 4.9 eV) [26], indicate nano-Schottky barriers are formed at the interface of tungsten oxide and gold or platinum NPs. Considering the direct relation of the depletion depth and surface potential barrier [27], it is likely that the functionalized sensors experience different depletion depths for the same reactive species at the surface, affecting the electrical properties of tungsten oxide. Estimation of the activation energy for the electrical conduction based on conductivity measurements between 190 and 300 ºC in air revealed different apparent energies for non-functionalized (0.22 eV), Au-functionalized (0.25 eV) and Pt-functionalized sensors (0.15 eV). The apparent energy for non-functionalized sensors is in good agreement with earlier results reported for tungsten oxide [28]. Moreover, the change in the apparent energy of functionalized sensors is consistent with our recent reports on the activation energy for electrical conduction of Au- and Pt-functionalized tungsten oxide grown in 'hot-wall' reactor [4b]. These results suggest gold and platinum NPs are effectively co-deposited with tungsten oxide by heating locally the microsensor, also, indicate the presence of strong electronic interaction between the NPs and the nanostructured support, particularly for Pt-functionalized structures.

3.5.Gas sensing response

Gas-sensing tests were carried out towards H_2, CO and EtOH, three analytes that could be involved in different processes, such as the production of hydrogen from fossil fuels, or the conversion of EtOH into H_2 in proton-exchange fuel cells [5d; 29].

To understand the effect of the temperature on the response of non-functionalized and functionalized sensors, gas-sensing tests to H_2, CO and EtOH, were performed at various temperatures, in the range from 160 to 390 ºC (the power consumption for these operating temperatures was about 16 and 60 mW, respectively). Overall, the sensor response showed an n-type semiconductor behavior, i.e. decreasing electrical resistance when exposed to these reducing gases. Besides, the sensor response displayed quite stable and reproducible responses along the test cycles showing standard errors below ±3% for operating temperatures equal or exceeding 220 °C, in contrast to those obtained below 220°C, which showed small and unsaturated responses with slower response and recovery times as typically noticed in MOX-based gas sensors at low temperatures. A comparison of the tendency of the sensor response with temperature for each microsensor (Figure 6) suggests the sensor response is influenced by the composition of the sensing film and the tested analyte. Also, it suggests that the temperatures for a maximum-sensor response magnitude for each analyte are shifted according to the composition of material. Consequently, results for non-functionalized sensors showed the highest sensor responses at operating temperatures between 280 ºC and 390 ºC to EtOH, and at 330 ºC and 390 ºC to H_2 and CO, respectively. Similarly, Pt-functionalized sensors showed the highest responses between 330°C and 390 ºC to H_2 and EtOH, and at 330 ºC to CO, whereas Au-functionalized sensors showed their highest responses at the same temperature (390 ºC) to H_2, CO or EtOH.

The relationship between the sensor response and concentration at 330°C for H_2 and 390°C for EtOH, and CO is illustrated in Figure 7. These results show an exponential

change of the response with respect to the gas concentrations, suggesting a saturation of the response as the analyte concentration increases, which represents a normal behavior in MOX-based gas sensors. Results in Figure 7 also show that the response of non-functionalized sensors is enhanced to H_2 and EtOH by its functionalization with gold NPs and platinum NPs, respectively, whereas results for CO show the opposite behavior.

From the results presented in Figure 6 and Figure 7 it is difficult to select one of these materials as the best option either for EtOH, H_2 or CO detection, due to the fact that the magnitude of response varies differently for each type of material with temperature. However, taking into account the higher operation temperatures, where the dynamics of the sensor response are faster (see section 2.7), results suggest that non-functionalized tungsten oxide sensors are more suitable to sense CO, whereas Au-functionalized sensors are better for EtOH and Pt-functionalized sensors for detecting H_2. This is in line with our previous observations for non-functionalized and functionalized tungsten oxide, grown in a 'hot-wall' reactor, in which it was noticed the same affinity between these materials and analytes [4b]. The slightly smaller response magnitudes for sensors fabricated via localized heating compared to those in 'hot-wall' reactor could be related to the differences (i.e. size of the membrane, heater design and heating material) of the microsensor platform [4b], although it is worth noting that the response registered with these sensors to H_2, CO and EtOH is in the same order of magnitude than those reported in the literature [17; 28; 30]. Figure 8 displays an example of the response and repeatability of the sensors to H_2, CO and EtOH operating at the maximum temperature studied (the base resistance of the sensors at this temperature were ~203KΩ for WO_{3-x} , ~427 KΩ for WO_{3-x}/Au and ~321 KΩ for WO_{3-x}/Pt, showing low drifts during the testing period with standard errors below ±7%).

Humidity tests were performed for CO at 390 °C in the presence of 50% and 90% of relative humidity (RH). Overall these results were characterized by stable baseline resistances with reproducible resistance changes when exposing the sensors to 500 ppm of CO, similarly to those observed for test under dry air (Figure 8). However, the sensor response showed different magnitudes, compared to those recorded for the same gas and concentration tested in dry air, and for instance, at 50 % of RH, the response of the sensors was increased by a 18 % for WO_{3-x}, 35 % for WO_{3-x}/Au and 140 % for WO_{3-x}/Pt.These results suggest humidity interferences for these sensors, as noticed before for other MOX-based sensors [5b; 12; 31].

3.6.Selectivity of the microsensors array

Gas-sensing tests show that single microsensors, either employing non-functionalized or functionalized nanostructures, present relatively high cross-sensitivities among H_2, CO and EtOH, which confirms that a selective detection of these analytes using only one sensing element is not possible. In contrast, the cross sensitivities for the same analytes (H_2, CO and EtOH) become much lower among different microsensors, including non-functionalized and functionalized elements, which suggest analytes could be selectively detected by correlating the response of these microsensors. Consequently, to evaluate the correlation between sensor responses and selectivity of the microsensors, a principal component analysis (PCA) was performed using an autoscaled pre-processing technique to the dataset of the sensor response replicates to each analyte and concentration (48 measurements × 3 variables). A visual appraisal of the discrimination of each analyte and its concentration using the array of microsensors (i.e. based in non-functionalized and functionalized with gold and platinum NPs) is depicted by the scores (Figure 9a), that is, the projections of measurements in an orthogonal base of PCs, and although the loading of each microsensor to the principal components (Figure 9b) show the sensors have a

certain degree of correlation, it can be noticed that the differences in the sensing properties of each sensor provide complementary information to discriminate H_2 and EtOH from CO. Carbon monoxide is a typical contaminant gas that arises in the production of H_2 from natural gas or ethanol (e.g. proton-exchange fuel cells) and its selective detection could be particularly important in this growing market, in which gas sensors based on semiconductors are attracting much interest.

3.7. Gas sensing dynamics

Figure 10 shows the response time as function of sensor operating temperature for each material and analyte. Overall, we observe the incorporation of additives in the support may have a positive or negative influence in the dynamics of the sensor response, with an analyte dependency. For instance for Au-functionalized sensors, the enhancement of the response time, relatively to non-functionalized sensors, to H_2 and EtOH may indicate that gold NPs act to catalyze detection of these analytes on tungsten oxide. In contrast, gold NPs act differently for CO with a catalysis potentially more efficient on non-functionalized structures compared to those functionalized with gold NPs. The results for Pt-functionalized structures may suggest a similar effect to that observed for CO and Au-functionalized structures, that is, having a poor catalytic effect for H_2, CO and EtOH, with the response time of these sensors being increased in comparison to their non-functionalized counterparts. These results (Figure 10) indicate that an enhancement in the dynamics of response does not necessarily imply an improvement in sensor response magnitude. A clear example is noticed for Pt-functionalized sensors, which show higher sensor response for H_2 compared to non-functionalized sensors, but similar response time. Analogously, for CO sensing, in which Pt-functionalized sensors show similar responses (between 160 and 300 °C) to those obtained with non-functionalized sensors, but with longer response times. This suggest that gold and platinum NPs at the surface of tungsten

oxide NSs could bring about different sensing mechanisms.

3.8.Gas sensing mechanism

The mechanisms explaining the role of additives in gas sensing are based on three ideas. The first, related to an enrichment of the MOX surface with reactive species through catalysis 'spill-over', the second, to changes in the chemical state of the additives with the analytes 'Fermi-level control' and the third, recently noticed in palladium and platinum NPs supported on SnO_2, that suggest a 'local/surface site effect' highly dependent on the distribution of additives at the surface of the MOX [32]. Although discrimination of the presence of these mechanisms and the degree of their contribution to the sensing response are not straightforward from current results, the electrical properties and the gas sensing dynamics of these structures might be giving some insight into the mechanism influencing the sensing properties of tungsten oxide nanostructures functionalized with gold and platinum NPs. For instance, the strong electronic interaction between the NPs and the nanostructured support noticed in section 2.4 suggests, particularly for Pt-functionalized structures, that the sensing mechanism of this material includes Fermi-level control. This effect is plausible as precious metal NPs, including platinum, may modify the Fermi level of the support due to the presence of oxidized states (at least at the shell surrounding NPs) [32a]. In contrast, the enhanced response times for Au-functionalized sensors when compared to non-functionalized sensors, for H_2 and EtOH (Figure 10), might be indicating that gold NPs enhance the response towards these analytes on tungsten oxide by a spill-over mechanism, as opposed to Pt-functionalized sensors.

In summary, results indicate AACVD induced by localized heating of microsensor devices is viable and enables the facile integration of nanostructures with microsystems. AACVD has demonstrated to be highly tolerant to the non-isothermal environments that

characterize localized heating, yielding uniform structures on the sensing active area of the devices and resulting in similar sensing properties to those observed for structures synthesized in a 'hot-wall' AACVD reactor.

4. Conclusions

Localized heating, via resistive microheaters, was satisfactorily employed for the AACVD growth of NSs (non-functionalized or functionalized tungsten oxide with gold or platinum NPs, with aspect ratios between 10 and 175) on gas sensing microsystems. The onset temperature for the formation of these structures on the sensing active area of the microsensors was found at 580 °C (i.e. the effective temperature in the sensing-active area of the microsensors), demonstrating that each microsensor provides suitable thermal conditions for the localized synthesis, via AACVD, of high quality functional NSs in the form of hollow nanotubes and nanoneedles (with similar characteristics to those obtained by using conventional AACVD method, i.e. in 'hot-wall' reactors). This method could be an effective route to fabricate arrays of microsensors with tunable functional properties within a single chip, avoiding the use of masks or intermediate thermal process steps for the integration of sensing nanomaterials, which may result in an economic improvement due to the optimization of material usage, the simplification of the processing steps and consequently the reduction of the processing time. The sensing devices fabricated using this method showed satisfactory sensitivities to H_2, CO and EtOH, with the highest outputs for non-functionalized tungsten oxide NSs showing a response of 4.3 to 80 ppm of CO, tungsten oxide functionalized with gold NPs showing a response of 7 to 80 ppm of EtOH, and tungsten oxide functionalized with platinum NPs showing a response of 3.6 to 80 ppm of H_2. Principal component analysis of the sensor response replicates to each gas and concentration suggested that the differences in the sensing properties of each element of the array provide the complementary information to discriminate H_2 and EtOH

from CO.

Acknowledgments

The support of the 'South Moravian Programme – SoMoPro' and the 'Ministerio de Economía y Competitividad' via grants 4SGA8678, TEC2012-32420, and TEC2013-48147 are gratefully acknowledged. Part of this research has used the infrastructure of the SIX Centre. E.L. is supported by the Catalan Institution for Research and Advanced Studies via the ICREA Academia Award.

References

[1] (a) A. Hierlemann, H. Baltes, CMOS-based chemical microsensors, *Analyst* 128 (2003) 15-28; (b) S.-W. Chiu, K.-T. Tang, Towards a Chemiresistive Sensor-Integrated Electronic Nose: A Review, *Sensors* 13 (2013) 14214-14247; (c) R. Bogue, Recent developments in MEMS sensors: a review of applications, markets and technologies, *Sensor Review* 33 (2013) 300-304; (d) S. Lakkis, R. Younes, Y. Alayli, M. Sawan, Review of recent trends in gas sensing technologies and their miniaturization potential, *Sensor Review* 34 (2014) 24-35.

[2] A. Vergara, R. Calavia, R.M. Vázquez, A. Mozalev, A. Abdelghani, R. Huerta, E.H. Hines, E. Llobet, Multifrequency Interrogation of Nanostructured Gas Sensor Arrays: A Tool for Analyzing Response Kinetics, *Anal Chem* 84 (2012) 7502-7510.

[3] (a) K.J. Choi, H.W. Jang, One-Dimensional Oxide Nanostructures as Gas-Sensing Materials: Review and Issues, *Sensors* 10 (2010) 4083-4099; (b) A. Gurlo, Nanosensors: Does crystal shape matter?, *Small* 6 (2010) 2077-2079.

[4] (a) T. Stoycheva, S. Vallejos, C. Blackman, S.J.A. Moniz, J. Calderer, X. Correig, Important considerations for effective gas sensors based on metal oxide nanoneedles films, *Sens. Actuator B* 161 (2012) 406-413; (b) S. Vallejos, P. Umek, T. Stoycheva, F. Annanouch, E. Llobet, X. Correig, P. De Marco, C. Bittencourt, C. Blackman, Single-Step Deposition of Au- and Pt-Nanoparticle-Functionalized Tungsten Oxide Nanoneedles Synthesized Via Aerosol-Assisted CVD, and Used for Fabrication of Selective Gas Microsensor Arrays, *Adv. Funct. Mater.* 23 (2013) 1313-1322.

[5] (a) X. Chen, C.K.Y. Wong, C.A. Yuan, G. Zhang, Nanowire-based gas sensors, *Sens. Actuator B* 177 (2013) 178-195; (b) A. Ponzoni, E. Comini, I. Concina, M. Ferroni, M. Falasconi, E. Gobbi, V. Sberveglieri, G. Sberveglieri, Nanostructured Metal Oxide Gas Sensors, a Survey of Applications Carried out at SENSOR Lab, Brescia (Italy) in the Security and Food Quality Fields, *Sensors* 12 (2012) 17023-17045; (c) Y. Liu, J. Parisi, X. Sun, Y. Lei, Solid-state gas sensors for high temperature applications - a review, *J. Mater. Chem. A* 2 (2014) 9919-9943; (d) M.G.S. Forum, MNT Gas Sensor Roadmap v3.0, (2006), http://www.gas-sensor-roadmap.com/.

[6] J. Huang, Q. Wan, Gas sensors based on semiconducting metal oxide one-dimensional nanostructures, *Sensors* 9 (2009) 9903-9924.

[7] B.D. Sosnowchik, L. Lin, O. Englander, Localized heating induced chemical vapor deposition for one-dimensional nanostructure synthesis, *J. Appl. Phys.* 107 (2010).

[8] S. Barth, R. Jimenez-Diaz, J. Sama, J. Daniel Prades, I. Gracia, J. Santander, C. Cane, A. Romano-Rodriguez, Localized growth and in situ integration of nanowires for device applications, *Chem. Commun.* 48 (2012) 4734-4736.

[9] E. Comini, C. Baratto, G. Faglia, M. Ferroni, A. Vomiero, G. Sberveglieri, Quasi-one dimensional metal oxide semiconductors: Preparation, characterization and application as chemical sensors, *Prog. Mater Sci.* 54 (2009) 1-67.

[10] (a) S. Vallejos, P. Umek, C. Blackman, AACVD Control parameters for selective deposition of tungsten oxide nanostrucutres, *J. Nanosci. Nanotechnol.* 11 (2011) 8214-8220; (b) S. Vallejos, T. Stoycheva, P. Umek, C. Navio, R. Snyders, C. Bittencourt, E. Llobet, C. Blackman, S. Moniz, X. Correig, Au nanoparticle-functionalised WO_3 nanoneedles and their application in high sensitivity gas sensor devices, *Chem. Commun.* 47 (2011) 565-567.

[11] S. Vallejos, R. Cumeras, C. Calaza, N. Sabate, E. Figueras, C. Cane, I. Gracia, Localized heating

to tungsten oxide nanostructures deposition on gas microsensor arrays via aerosol assisted CVD, *Solid-State Sensors, Actuators and Microsystems (TRANSDUCERS & EUROSENSORS XXVII), 2013 Transducers & Eurosensors XXVII: The 17th International Conference on* (2013) 1166-1169.

[12] G.F. Fine, L.M. Cavanagh, A. Afonja, R. Binions, Metal Oxide Semi-Conductor Gas Sensors in Environmental Monitoring, *Sensors* 10 (2010) 5469-5502.

[13] (a) S. Vallejos, V. Khatko, K. Aguir, K.A. Ngo, J. Calderer, I. Gràcia, C. Cané, E. Llobet, X. Correig, Ozone monitoring by micro-machined sensors with WO3 sensing films, *Sens. Actuator B* 126 (2007) 573-578; (b) A. Labidi, C. Jacolin, M. Bendahan, A. Abdelghani, G. J., K. Aguir, M. Maaref, Impedance spectroscopy onWO_3 gas sensor, *Sens. Actuator B* 106 (2005) 713-718.

[14] (a) R. Calavia, A. Mozalev, R. Vazquez, I. Gracia, C. Cané, R. Ionescu, E. Llobet, Fabrication of WO_3 nanodot-based microsensors highly sensitive to hydrogen, *Sens. Actuators B* 149 (2010) 352-361; (b) M. Ahsan, M.Z. Ahmad, T. Tesfamichael, J. Bell, W. Wlodarski, N. Motta, Low temperature response of nanostructured tungsten oxide thin films toward hydrogen and ethanol, *Sens. Actuator B* 173 (2012) 789-796.

[15] (a) L.F. Reyes, A. Hoel, S. Saukko, P. Heszler, V. Lantto, C.G. Granqvist, Gas sensor response of pure and activated WO_3 nanoparticle films made by advanced reactive gas deposition, *Sens. Actuators B* 117 (2006) 128-134; (b) M. Stankova, X. Vilanova, J. Calderer, E. Llobet, P. Ivanov, I. Gràcia, C. Cané, X. Correig, Detection of SO_2 and H_2S in CO_2 stream by means of WO_3-based micro-hotplate sensors, *Sens. Actuators B* 102 (2004) 219-225.

[16] Y. Li, X. Su, J. Jian, J. Wang, Ethanol sensing properties of tungsten oxide nanorods prepared by microwave hydrothermal method, *Ceram. Int.* 36 (2010) 1917-1920.

[17] S. Vallejos, V. Khatko, J. Calderer, I. Gracia, C. Canè, E. Llobet, X. Correig, Micro-machined WO_3-based sensors selective to oxidizing gases, *Sens. Actuator B* 132 (2008) 209-215.

[18] S. Ashraf, C.S. Blackman, R.G. Palgrave, S.C. Naisbitt, I.P. Parkin, Aerosol assisted chemical vapour deposition of WO_3 thin films from tungsten hexacarbonyl and their gas sensing properties, *J. Mater. Chem.* 17 (2007) 3708-3713.

[19] S. Vallejos, I. Gràcia, E. Figueras, C. Cané, Catalyst-Free Vapor-Phase Method for Direct Integration of Gas Sensing Nanostructures with Polymeric Transducing Platforms, *Journal of Nanomaterials* 2014 (2014) 9.

[20] S. Da-Shan, S. Lei, S. Ji-Rong, S. Bao-Gen, Local resistance switching at grain and grain boundary surfaces of polycrystalline tungsten oxide films, *Nanotechnology* 22 (2011) 254008.

[21] C.K. Tsung, W.B. Hong, Q.H. Shi, X.S. Kou, M.H. Yeung, J.F. Wang, G.D. Stucky, Shape- and Orientation-Controlled Gold Nanoparticles Formed within Mesoporous Silica Nanofibers, *Adv. Funct. Mater.* 16 (2006) 2225-2230.

[22] J.M. Kim, H.-I. Joh, S.M. Jo, D.J. Ahn, H.Y. Ha, S.-A. Hong, S.-K. Kim, Preparation and characterization of Pt nanowire by electrospinning method for methanol oxidation, *Electrochim. Acta* 55 (2010) 4827-4835.

[23] J. Décobert, R. Guillamet, C. Mocuta, G. Carbone, H. Guerault, Structural characterization of selectively grown multilayers with new high angular resolution and sub-millimeter spot-size x-ray diffractometer, *Journal of Crystal Growth* 370 (2013) 154-156.

[24] (a) C. Santato, M. Odziemkowski, M. Ulmann, J. Augustynski, Crystallographically Oriented Mesoporous WO_3 Films: Synthesis, Characterization, and Applications, *J. Am. Chem. Soc.* 123 (2001) 10639-10649; (b) Y.-T. Hsieh, M.-W. Huang, C.-C. Chang, U.-S. Chen, H.-C. Shih, Growth and optical properties of uniform tungsten oxide nanowire bundles via a two-step heating process by thermal evaporation, *Thin Solid Films* 519 (2010) 1668-1672; (c) J.Y. Luo, S.Z. Deng, Y.T. Tao, F.L. Zhao, L.F. Zhu, L. Gong, J. Chen, N.S. Xu, Evidence of Localized Water Molecules and Their Role in the Gasochromic Effect of WO3 Nanowire Films, *J. Phys. Chem. C* 113 (2009) 15877-15881.

[25] T. Sergio, Work function, electronegativity, and electrochemical behaviour of metals: II. Potentials of zero charge and "electrochemical" work functions, *J. Electroanal. Chem. Interfacial Electrochem.* 33 (1971) 351-378.

[26] T. He, J. Yao, Photochromic materials based on tungsten oxide, *J. Mater. Chem.* 17 (2007) 4547-4557.

[27] N. Yamazoe, K. Shimanoe, Theory of power laws for semiconductor gas sensors, *Sens. Actuator B* 128 (2008) 566-573.

[28] S. Ashraf, C.S. Blackman, S.C. Naisbitt , I.P. Parkin, The gas-sensing properties of WO_{3-x} thin films deposited via the atmospheric pressure chemical vapour deposition (APCVD) of WCl_6 with ethanol, *Meas. Sci. Technol.* 19 (2008) 1-9.

[29] J.L. Silveira, L.B. Braga, A.C.C. de Souza, J.S. Antunes, R. Zanzi, The benefits of ethanol use for hydrogen production in urban transportation, *Renew. Sustain. Energ. Rev.* 13 (2009) 2525-2534.

[30] (a) M. Stankova, X. Vilanova, J. Calderer, E. Llobet, J. Brezmes, I. Gràcia, C. Cané, X. Correig,

Sensitivity and selectivity improvement of rf sputtered WO_3 microhotplate gas sensors, *Sens. Actuator B* 113 (2006) 241-248; (b) D.J. Smith, J.F. Vatelino, R.S. Falconer, E.L. Wittman, Stability, sensitivity and selectivity of tungsten trioxide films for sensing applications, *Sens. Actuator B* 13 (1993) 264-268; (c) C. Zhang, A. Boudiba, C. Navio, C. Bittencourt, M.-G. Olivier, R. Snyders, M. Debliquy, Highly sensitive hydrogen sensors based on co-sputtered platinum-activated tungsten oxide films, *Int. J. Hydrogen Energy* 36 (2011) 1107-1114.

[31] F. Hernández-Ramírez, A. Tarancón, O. Casals, J. Arbiol, A. Romano-Rodríguez, J.R. Morante, High response and stability in CO and humidity measures using a single SnO2 nanowire, *Sensors and Actuators B: Chemical* 121 (2007) 3-17.

[32] (a) J.F. McAleer, P.T. Moseley, J.O.W. Norris, D.E. Williams, B.C. Tofield, Tin dioxide gas sensors. Part 2.-The role of surface additives, *J. Chem. Soc., Faraday Trans. 1: Physical Chemistry in Condensed Phases* 84 (1988) 441-457; (b) D. Koziej, M. Hubner, N. Barsan, U. Weimar, M. Sikora, J.-D. Grunwaldt, Operando X-ray absorption spectroscopy studies on Pd-SnO_2 based sensors, *Phys. Chem. Chem. Phys.* 11 (2009) 8620-8625; (c) M. Hübner, D. Koziej, M. Bauer, N. Barsan, K. Kvashnina, M.D. Rossell, U. Weimar, J.-D. Grunwaldt, The Structure and Behavior of Platinum in SnO_2-Based Sensors under Working Conditions, *Angew. Chem. Int. Ed.* 50 (2011) 2841-2844.

Figure captions

Figure 1. Schematic view (not to scale) of the microsensor platform section (a) and photograph of an individual microsensor platform showing the sensing-active area (b). Array of microsensors mounted on a standard TO-8 package (c).

Figure 2. Simulated thermal profile (a) and temperature distribution (b) at the sensing active area (red area).

Figure 3. Film morphology observed by SEM images at low (a) and high (b and c) magnification.

Figure 4. TEM of the non-functionalized (a) and functionalized NSs with gold (b and d) and platinum NPs (c and e).

Figure 5. XRD patterns (a) and Raman spectra (b) recorded on the microsensors based on non-functionalized (WO_{3-x}) and functionalized tungsten oxide NSs with gold (WO_{3-x}/Au) and platinum (WO_{3-x}/Pt) NPs.

Figure 6. Sensor responses and error bars to 500 ppm of H_2, 500 ppm of CO and 80 ppm of EtOH as a function of the operating temperature.

Figure 7. Sensor responses to various concentrations of H_2 (20, 80, 200, 500 ppm), CO (40, 80, 200, 500 ppm) and EtOH (20, 40, 60, 80 ppm)

Figure 8. Film-resistance changes towards H_2, CO and EtOH, at 390 °C

Figure 9. PCA analysis of the sensor response displaying the scores or projections of measurements in an orthogonal base of PCs (a) and loading of each sensor to the PCs (b)

Figure 10. Response time as a function of sensor operating temperature

Figures

2

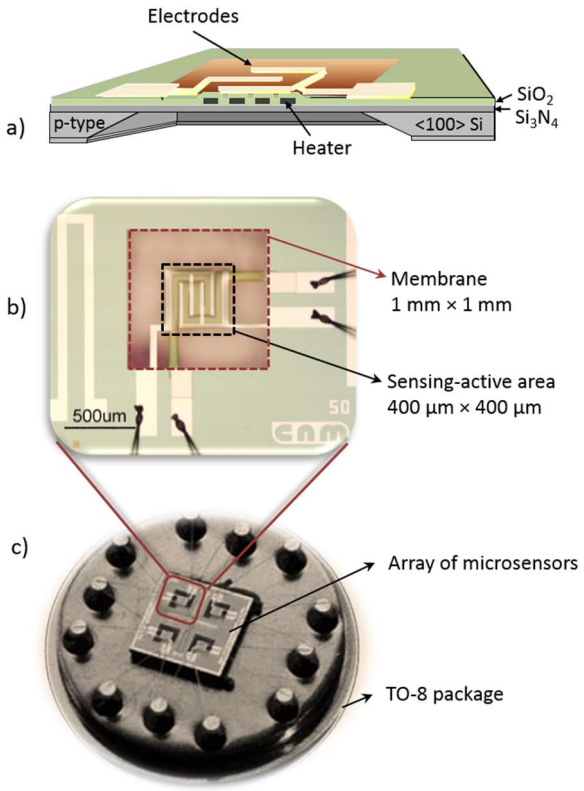

4 Figure 1.

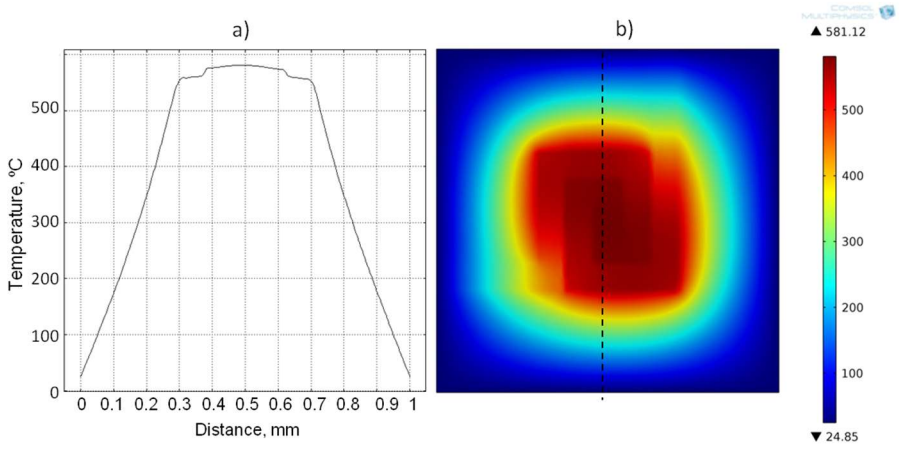

6 Figure 2.

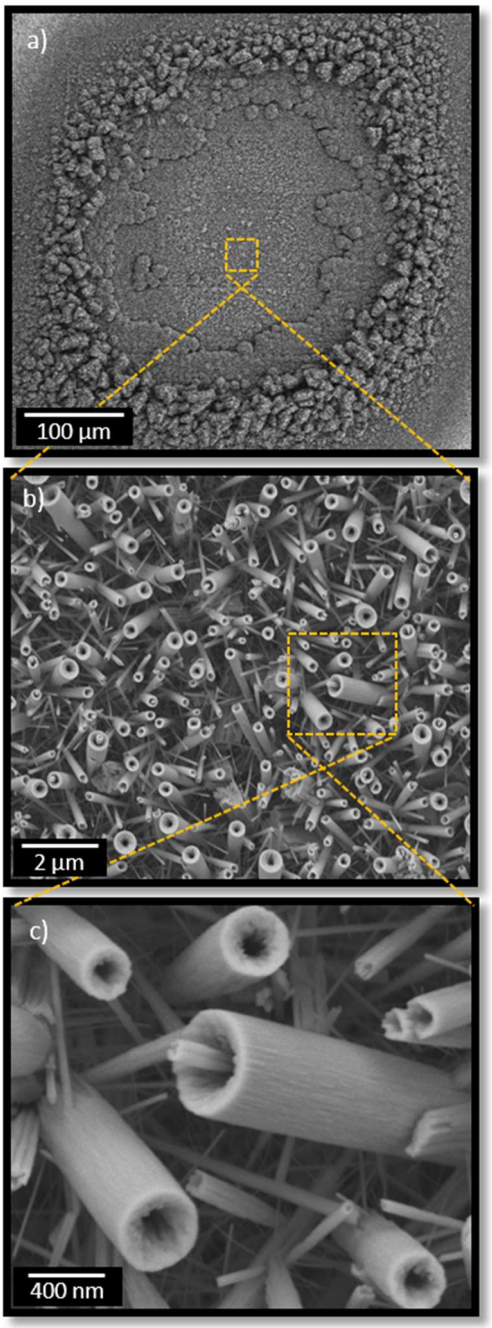

Figure 3.

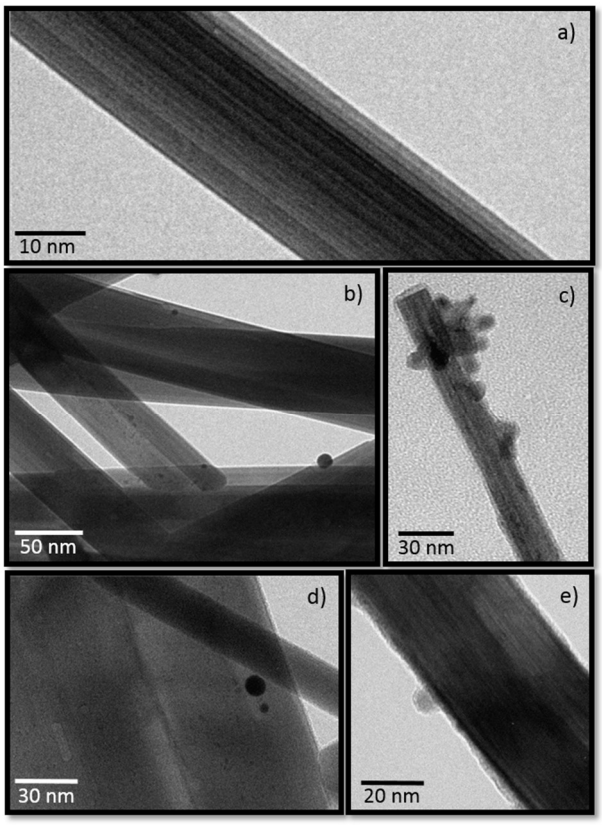

2 Figure 4.

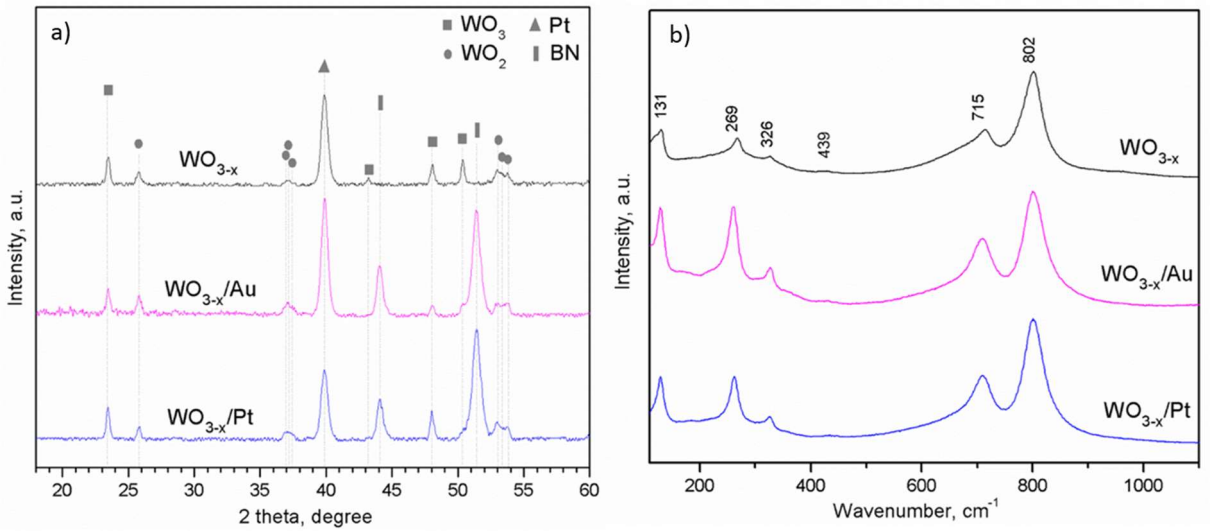

4 Figure 5.

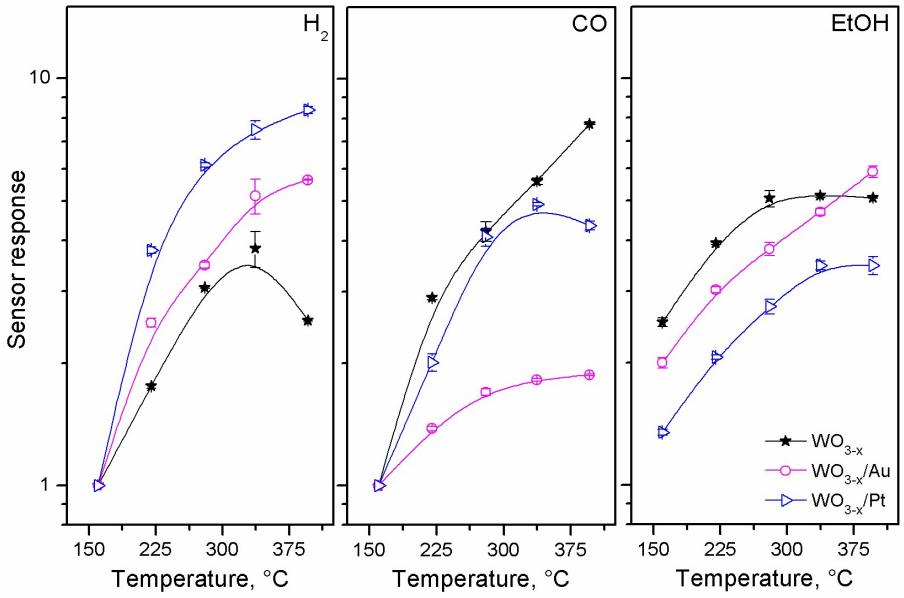

Figure 6.

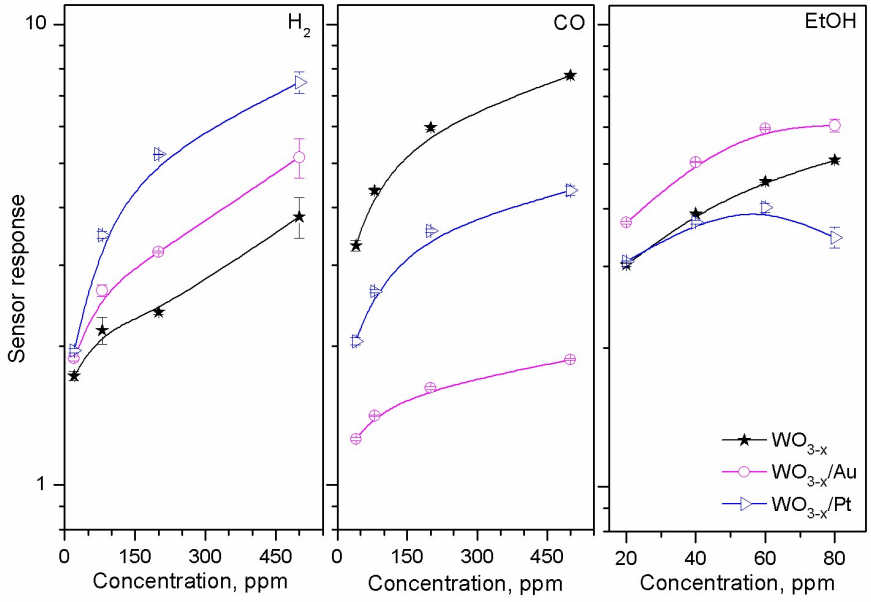

Figure 7.

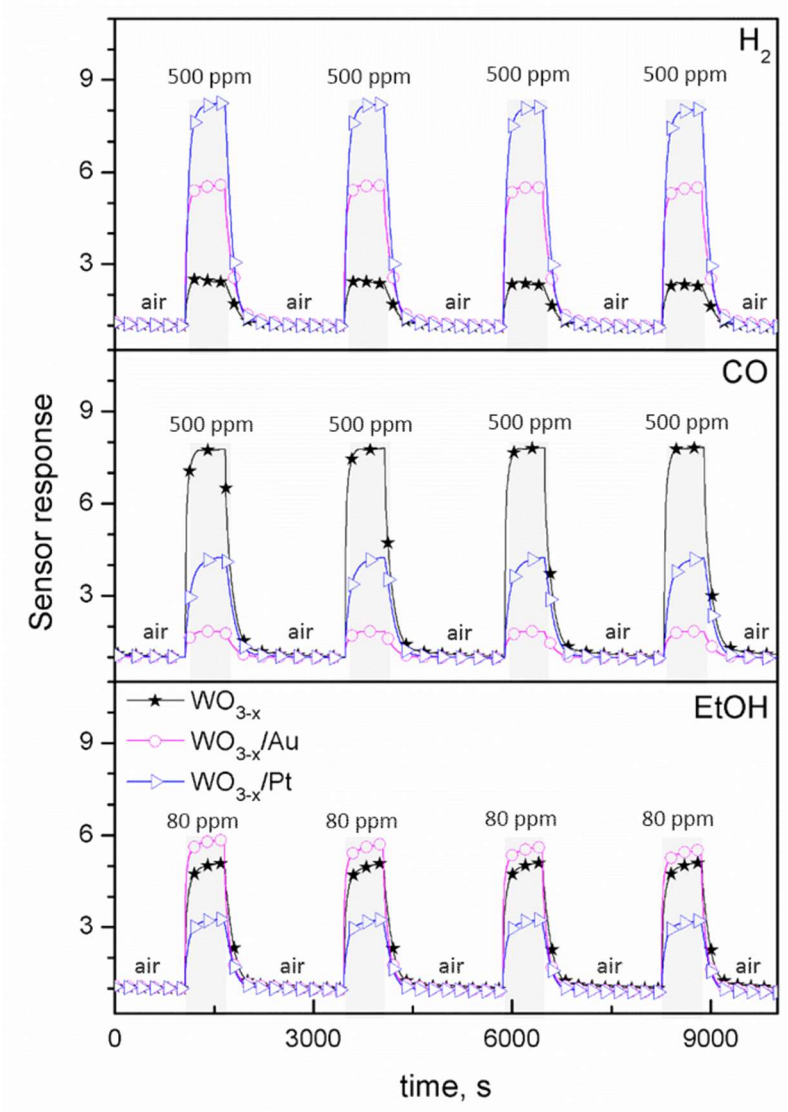
H2
CO
EtOH
500 ppm
80 ppm
air
WO3-x
WO3-x/Au
WO3-x/Pt
Sensor response
time, s
0
3000
6000
9000
3
6
9

Figure 8.

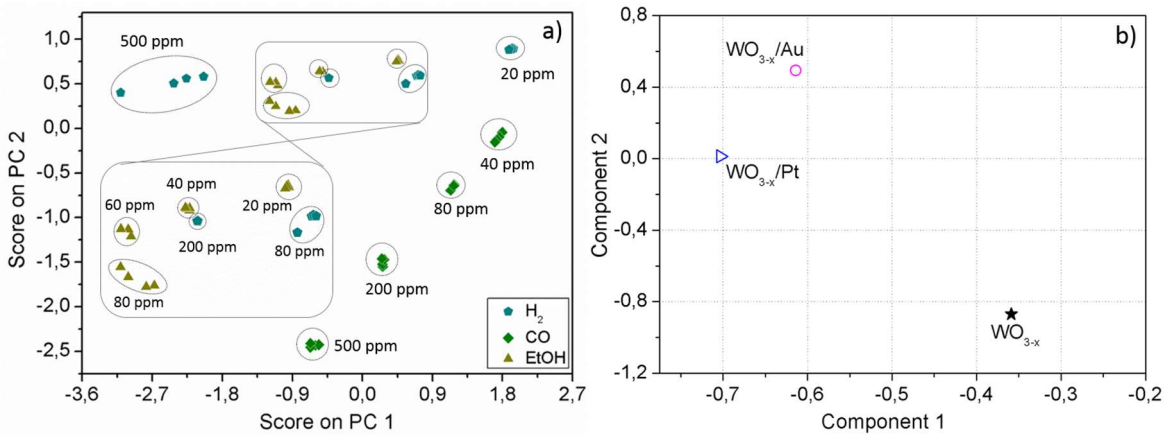

2 Figure 9.

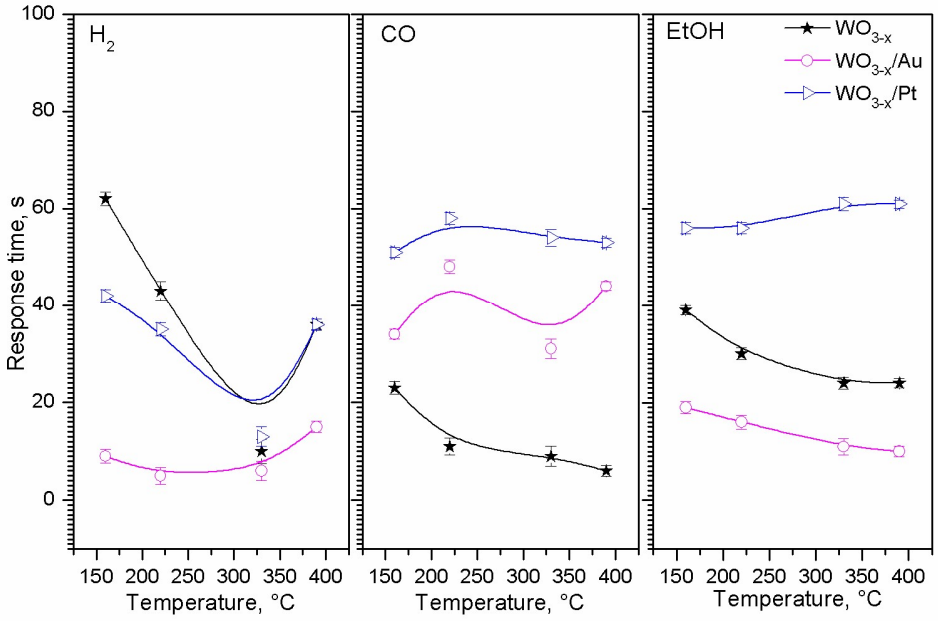

4 Figure 10.